



# Boosting photo-Fenton process enabled by ligand-to-cluster charge transfer excitations in iron-based metal organic framework

Wen-Qiang Li<sup>a,1</sup>, Yi-Xuan Wang<sup>a,1</sup>, Jia-Qi Chen<sup>a</sup>, Nan-Nan Hou<sup>a,c,\*</sup>, Yuan-Ming Li<sup>b</sup>,  
Xiao-Cheng Liu<sup>a</sup>, Rong-Rong Ding<sup>a</sup>, Guan-Nan Zhou<sup>a</sup>, Qi Li<sup>a</sup>, Xiao-Guo Zhou<sup>b</sup>, Yang Mu<sup>a,\*\*</sup>

<sup>a</sup> CAS Key Laboratory of Urban Pollutant Conversion, Department of Environmental Science and Engineering, University of Science and Technology of China, Hefei 230026, China

<sup>b</sup> Department of Chemical Physics, University of Science and Technology of China, Hefei 230026, China

<sup>c</sup> Department of Physics, Hefei Normal University, Hefei 230601, China

## ARTICLE INFO

### Keywords:

Photo-Fenton

Fe-based metal organic frameworks

Ligand-to-cluster charge transfer excitations

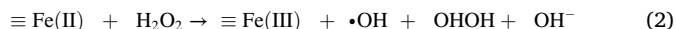
Fe(III)/Fe(II) transformation

## ABSTRACT

Iron-based metal organic frameworks (MOFs) are widely adopted to mediate heterogeneous photo-Fenton reaction, but poor charge separation efficiency in iron-oxo clusters of MOF usually results in the dull Fe(III)/Fe(II) transformation. In this study, ligand-to-cluster charge transfer (LCCT) excitations were first introduced to photo-Fenton process toward accelerating Fe(III)/Fe(II) transformation by constructing new iron-based MOF nanorods with porphyrin ligand (Fe-TCPP). Fe-TCPP with LCCT excitations showed a maximum kinetic constant of 0.23 min<sup>-1</sup> for ciprofloxacin (CIP) degradation at neutral pH under visible light irradiation, which is remarkably better than most of the state-of-the-art photocatalysts. Experimental and theoretical analyses collaboratively verify that LCCT excitations within Fe-TCPP dramatically accelerate Fe(III)/Fe(II) transformation, which generate more •OH for quick CIP elimination. Additionally, this LCCT excitations strategy is also effective for the photo-Fenton-like system induced by copper-based MOFs. Our study presents a novel strategy to intensify MOFs based photo-Fenton/Fenton-like processes, upon which the high-efficiency contaminant removal is expected.

## 1. Introduction

Recently, photo-Fenton process emerging as an advanced oxidation technology has been used for contaminants removal from water such as antibiotics, where generation of hydroxyl radicals (•OH) makes dominant contribution since its highest oxidative potential ( $E_0 = 1.9\text{--}2.7\text{ V}$ ) [1–4]. The fundamental of photo-Fenton process involves in driving Fe(III)/Fe(II) conversion induced by virtue of photoelectrons derived from light-responsive photocatalysts, following a common reaction of [5].



In this context, a variety of Fe-containing photocatalysts, such as FeO(OH), hematite and metal organic frameworks (MOF), were employed to initiate photo-Fenton reaction [2,3,6].

Among those photocatalysts, iron-based MOFs, such as MIL-100(Fe), featuring low toxicity, stable and abundant iron-oxo (Fe-O) cluster motifs that can serve as active sites to activate H<sub>2</sub>O<sub>2</sub> by Fe(III)/Fe(II) cycle process, are usually used to mediate the photo-Fenton process [7–9]. However, the separation efficiency of photogenerated carriers remains low due to the rapid electron-hole recombination in a single Fe-O cluster within iron-based MOF under visible light irradiation, which subsequently leads to sluggish Fe(III)/Fe(II) transformation process [6–8]. Recent advances show that most efforts are dedicated to introducing inorganic semiconductors or co-catalyst into the iron-based MOF structure, such as titanium dioxide and MXene, which could help to suppress the recombination process of photogenerated carriers in a single Fe-O cluster benefited from the heterostructure [6,10,11]. Nevertheless, the inherent wide band gap and poor electron conductivity of the metal oxides mentioned above may disable their further applications because of limited optical responsiveness and adverse

\* Corresponding author at: CAS Key Laboratory of Urban Pollutant Conversion, Department of Environmental Science and Engineering, University of Science and Technology of China, Hefei 230026, China.

\*\* Corresponding author.

E-mail addresses: [hounan@ustc.edu.cn](mailto:hounan@ustc.edu.cn) (N.-N. Hou), [yangmu@ustc.edu.cn](mailto:yangmu@ustc.edu.cn) (Y. Mu).

<sup>1</sup> These authors contributed equally to this work.

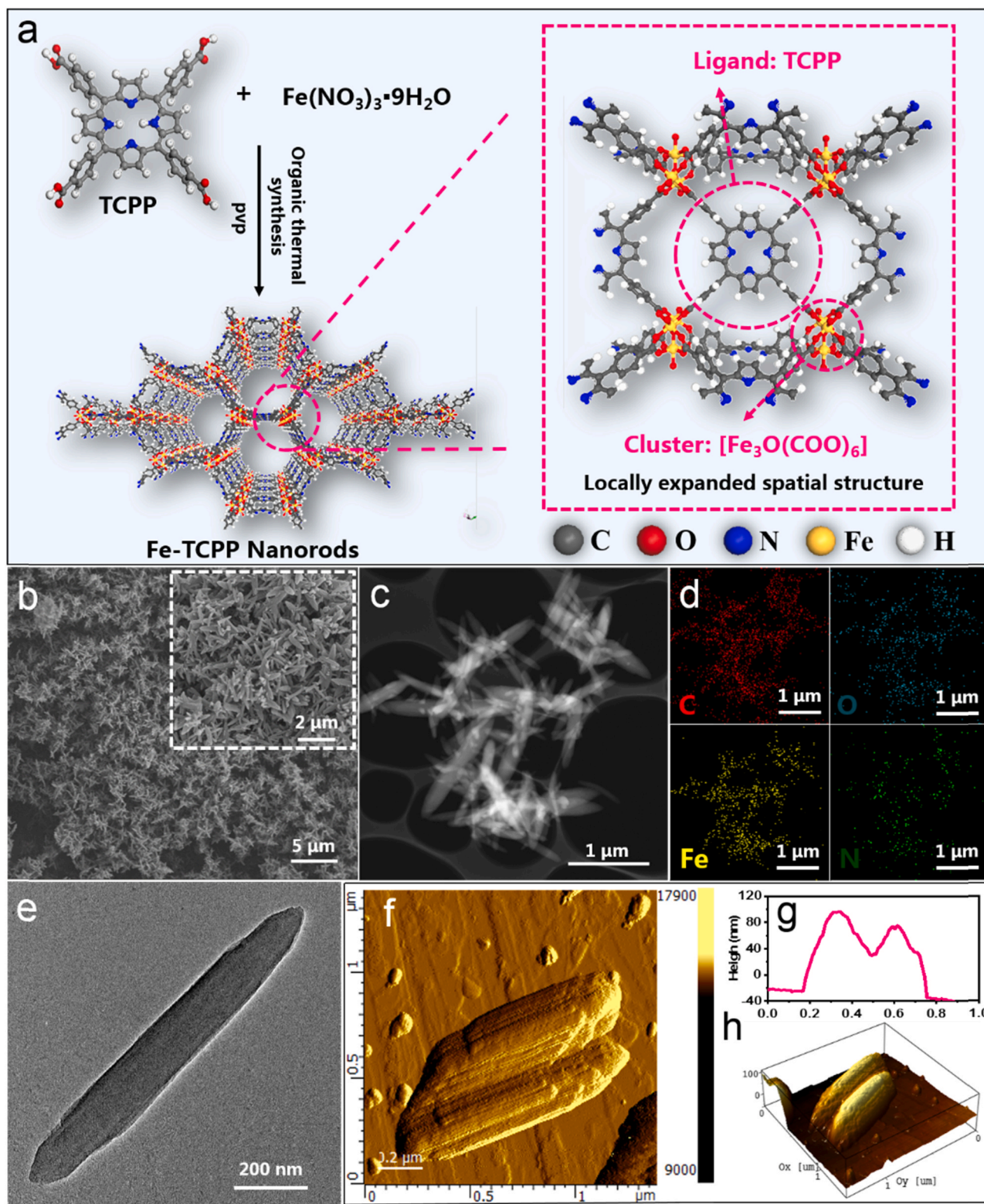


**Fig. 1.** Schematic illustration of Fe-TCPP formation and locally expanded spatial structure (a); SEM (b) and TEM images of Fe-TCPP (c) and (e); EDS mapping images of Fe-TCPP (d); AFM images of Fe-TCPP (f); Height profile of Fe-TCPP (g); Three-dimensional morphologic image of Fe-TCPP (h).

carrier migration rates [12]. Besides, it is well known that the synthesis of Mxene usually requires harsh conditions and complex steps, such as hydrofluoric acid etching and intercalation scheme [13,14]. Additionally, there was a serious layer stacking phenomenon for few-layer Mxene because of its high surface energy, which would negatively affects electron migration rate in practical applications [15].

In addition to the single cluster excitation process within MOFs, it has generally received more attention in the field of photocatalysis involving the interaction between ligands and clusters to enhance photocatalytic performance [16,17]. In this regard, ligand-to-cluster charge transfer (LCCT) excitations induced by the well-matched molecular orbitals between cluster and ligand in MOFs, constitutes the fundamental

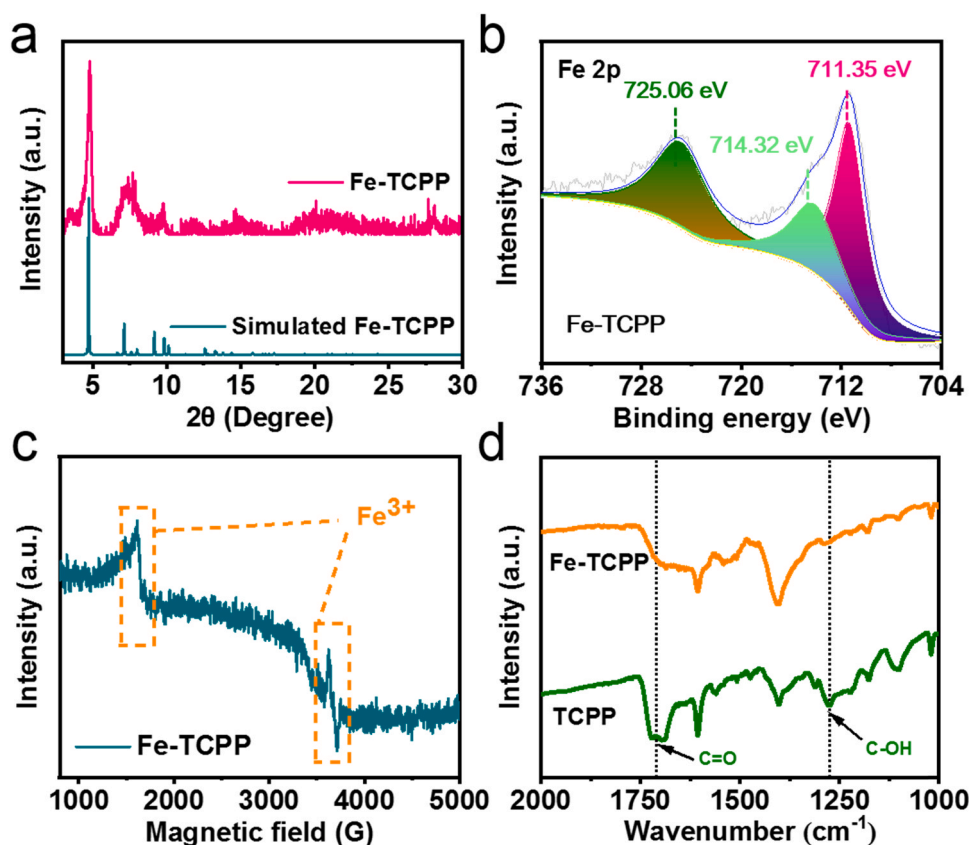


Fig. 2. XRD patterns of Fe-TCPP (a); Fe 2p XPS spectra of Fe-TCPP (b); Room-temperature EPR spectra of Fe-TCPP under dark (c); FT-IR spectra of Fe-TCPP (d).

reason for the photocatalytic activity over some MOFs [18,19]. That is, more charge-separated-state species are produced as a result of valid charge separation, which serve as active species to participate in the catalytic reactions [19,20]. Typically, a representative MOF, PCN-222, composed of Zr-oxo clusters and porphyrin (5, 10, 15, 20-tetra(4-carboxyphenyl)porphyrin = H<sub>2</sub>TCPP, named as TCPP) ligands, was employed to execute photocatalytic oxidative reaction toward coupling of amines [21]. Under visible light irradiation, the electrons from TCPP ligand transfer to Zr-oxo clusters to form a Zr-oxo active intermediate through LCCT excitations, which further combine adsorbed oxygen molecule to form a series of reactive oxygen species (ROS), and finally contribute to improved photocatalytic performance. Besides, Li and his co-workers demonstrated Zr(IV) within Zr-oxo clusters was reduced to Zr(III) in PCN-222 via LCCT excitations process under illumination, which further promoted hydrogen generation [22]. Inspired by above processes, introducing LCCT excitations to the iron-based MOF as an additional pathway for valid charge separation, is expected to promote the efficiency of the photo-Fenton process. As far as we know, however, potential use and the underline mechanism involving LCCT excitations toward accelerating sluggish Fe(III)/Fe(II) transformation in heterogeneous photo-Fenton reactions remains unexplored.

Herein, a new type of iron-based MOF (Fe-TCPP) nanorods consisting of TCPP ligands and Fe-O cluster (Fe<sub>3</sub>O(COO)<sub>6</sub>) was initially synthesized using the surfactant-assisted solvothermal procedure in order to introduce LCCT excitations [23]. Basic morphology and structure information of Fe-TCPP nanorods were explored by a series of characterizations. Afterwards, the performance of Fe-TCPP nanorods mediated photo-Fenton systems was systematically evaluated through a large number of degradation experiments of ciprofloxacin (CIP). Subsequently, both quenching experiments and the electron paramagnetic resonance (EPR) spectroscopy were adopted to identify dominating ROS in the Fe-TCPP nanorods mediated photo-Fenton system. More importantly, we combined in situ low-temperature EPR spectroscopy and

density functional theory (DFT) calculations to explore the potential LCCT excitations in Fe-TCPP nanorods, as well as its effect on the generation of ROS in the photo-Fenton system. In particular, the nano-second time-resolved transient absorption (NTA) spectroscopy as a robust tool was resorted to reveal the impact of LCCT excitations on the Fe(III)/Fe(II) transformation by capturing the changes of charge-separated species in the photo-Fenton system.

## 2. Experimental section

### 2.1. Chemicals and agents

All commercial reagents were used directly without further purification steps unless otherwise mentioned. Iron(III) nitrate nonahydrate (Fe(NO<sub>3</sub>)<sub>3</sub>·9H<sub>2</sub>O), polyvinylpyrrolidone (PVP, MW = 40,000), trifluoroacetic acid (TFA), N,N-Dimethylformamide (DMF), ethanol (EtOH), methanol (MeOH), tetrahydrofuran (THF), acetonitrile (C<sub>2</sub>H<sub>3</sub>N), hydrochloric acid (HCl, 37%), H<sub>2</sub>O<sub>2</sub> (30%), deionized water (H<sub>2</sub>O), CIP (C<sub>17</sub>H<sub>18</sub>FN<sub>3</sub>O<sub>3</sub>), sodium acetate trihydrate (NaOOCCH<sub>3</sub>·3H<sub>2</sub>O), methyl 4-formylbenzoate (C<sub>9</sub>H<sub>8</sub>O<sub>3</sub>), pyrrole, potassium hydroxide (KOH). Both TCPP and Fe<sub>3</sub>O(COO)<sub>6</sub> were synthesized following reported procedures [24,25].

### 2.2. Preparation of Fe-TCPP

Briefly, Fe-TCPP nanorods were synthesized by a simple surfactant-assisted solvothermal procedure [23]. Firstly, dispersion A containing 4.0 mg Fe(NO<sub>3</sub>)<sub>3</sub>·9H<sub>2</sub>O, 10 mg PVP, 40 μL TFA, 9 mL DMF and 3 mL EtOH, was subjected to ultrasonic treatment for 30 min. Dispersion B comprising 4.4 mg TCPP, 3 mL DMF and 1 mL EtOH, was also ultrasonicated for 30 min. Secondly, A and B were mixed and further sonicated for 15 min, which was then placed in a Teflon-lined autoclave at 90 °C for 24 h. The resultant solid material was successively washed



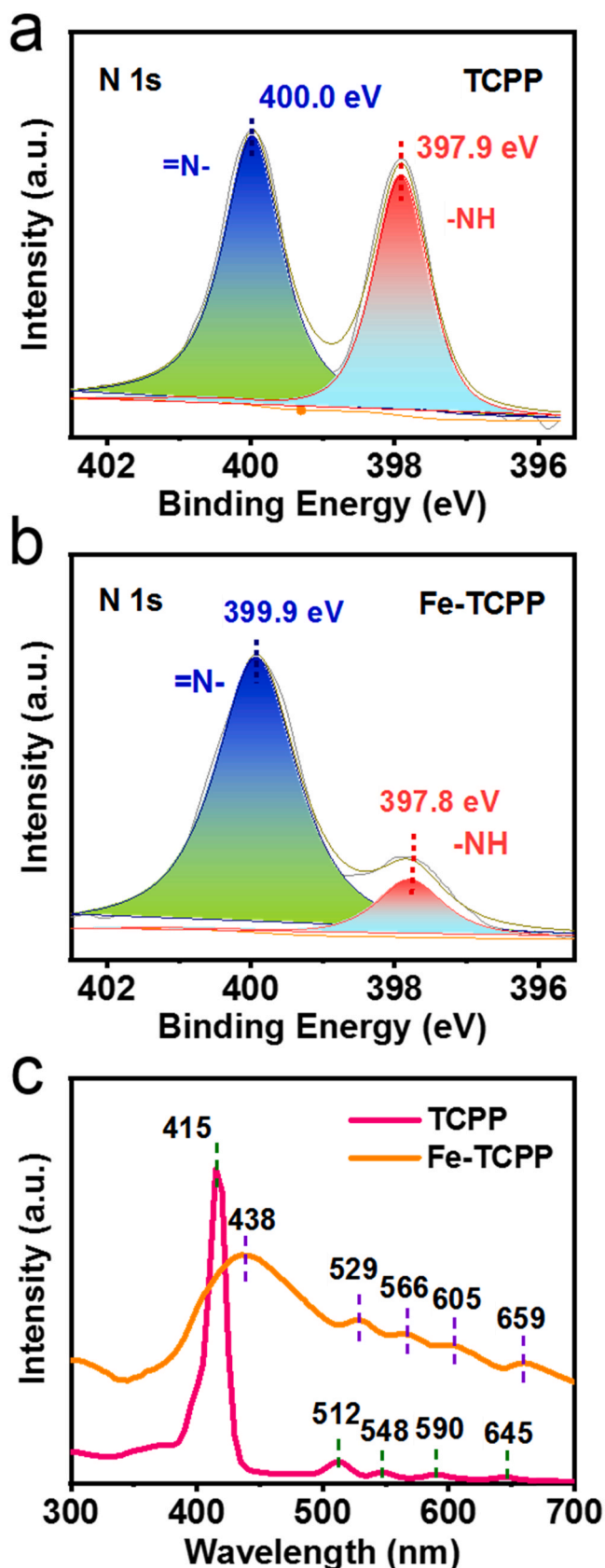


Fig. 3. N 1s XPS spectra of TCP (a) and Fe-TCP (b); Full-band scanning of TCP and Fe-TCP under ultraviolet-visible light (c).

with DMF and deionized water as well as acetone for three times, and finally dried in the vacuum oven at 60 °C overnight.

### 2.3. Characterizations

The details related to material characterizations are described in the Supporting Information (SI), including X-ray diffraction pattern (XRD), X-ray photoelectron spectroscopy (XPS) spectra, scanning electron microscopy (SEM) and field-emission transmission electron microscope (FETEM), etc.

In order to track the real-time charge separation process of the photocatalysts after photoexcitation, the NTA spectra were recorded with a home-built laser flash photolysis system [26]. The second harmonic 532 nm of a Q-Switched Nd: YAG laser (Dawa-100, Beamtech) was used as the pulsed excitation light (pulse duration: 8 ns, repetition rate: 10 Hz, pulse energy <10 mJ/pulse). A 500 W Xenon lamp was employed as the probing light, and quartz cuvette (10 mm × 10 mm) with light transmission on all sides was perpendicularly placed with the pulsed laser and probing light. A monochromator equipped with a photomultiplier was used to record transient absorption signal within a wavelength range of 330–1100 nm. The typical spectral resolution was less than 1 nm and the kinetic curve of charge-separated-states species was averaged by multi-shots and recorded with an oscilloscope (TDS3052B, Tektronix). All the materials after fully grinding were uniformly dispersed in a 4 mL transparent quartz cuvette sample cell using acetonitrile with a concentration of 60 mg L<sup>-1</sup>, and the experimental process was carried out at room temperature unless otherwise mentioned. The lifetime of charge-separated-states species were obtained by the nanosecond transient absorption kinetics diagram based on single exponential fitting Eq. (3) [27].

$$y = y_0 + A_1 e^{-\frac{x - x_0}{\tau}} \quad (3)$$

where  $y$ ,  $x$ ,  $y_0$  and  $x_0$  stand for the difference in absorbance before and after excitation light irradiation ( $\Delta O.D.$ ), delay time and the baselines, respectively;  $A_1$  is amplitude of the observed curve;  $\tau$  represents the experimental decay lifetime of charge-separated-states species [28].

### 2.4. Photo-Fenton experiments and analytical procedures

All CIP degradation experiments were carried out under visible light irradiation using a 300 W xenon lamp light source with the 420 nm cutoff filter at room temperature. In detail, 3.0 mg of the catalysts (60 mg L<sup>-1</sup>) was dispersed in 50 mL 25 mg L<sup>-1</sup> CIP solution after rapid stirring with the initial pH adjusted to 6.96 using 0.1 M KOH and HCl. The above dispersion was placed in the dark for 40 min to complete adsorption-desorption equilibrium after 25  $\mu$ L H<sub>2</sub>O<sub>2</sub> (5 mM) was injected. The photo-Fenton experiment was initiated when the whole system was exposed to the appropriate intensity of visible light (300 W), where the system temperature was kept at 25 °C by the constant addition of condensation water. Afterwards, 1.5 mL of the suspension was collected and further centrifuged at 15,000 rpm for 1 min to obtain the supernatant at a given time interval. In addition, the effects of pH and H<sub>2</sub>O<sub>2</sub> concentration on the photo-Fenton performance also followed the above experimental processes, except for changing H<sub>2</sub>O<sub>2</sub> concentration and initial pH of CIP solution to a specific value. The photocatalysts were collected at the end of each experiment by centrifugation, following by washing and drying operations for the cycle test.

The concentration of CIP in the system was determined using high performance liquid chromatography (HPLC, 1260 Infinity, Agilent Inc., U.S.A.) equipped with an Agilent HC-C18 reversed-phase column (5  $\mu$ m, 4.6 mm × 250 mm) at 30 °C and a UV-DAD detector (278 nm). The mobile phase consists of 75% water (containing 0.3% formic acid) and 25% acetonitrile with a flow rate of 1.0 mL min<sup>-1</sup>. Besides, the signal of  $\cdot$ OH was trapped by 20 mM DMPO and further detected through a JEOL JES-FA200 under visible light radiation at 298 K. The signal of high-spin



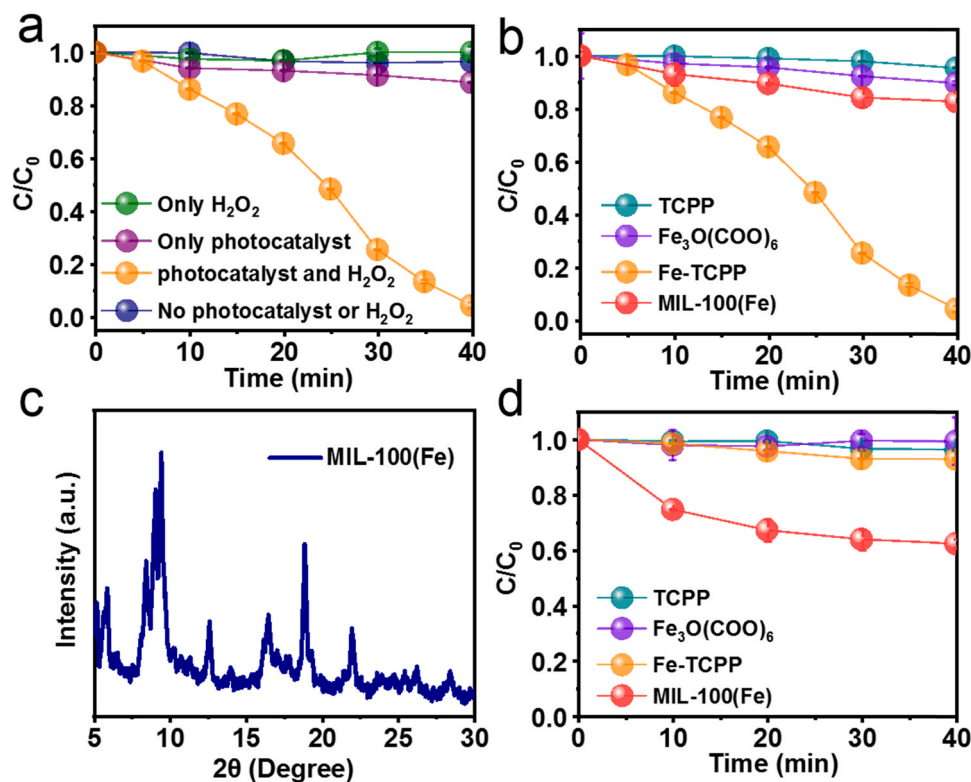


Fig. 4. Time profiles of CIP degradation efficiency over different systems (a) and various photocatalysts (b) at  $25 \pm 2^\circ\text{C}$  under visible light irradiation; XRD patterns of MIL-100(Fe) (c); Experimental studies on the adsorption of CIP over different photocatalysts under dark conditions (d). The initial concentrations of CIP and  $H_2O_2$  were  $25\text{ mg L}^{-1}$  and  $5\text{ mmol L}^{-1}$ , respectively. The catalyst concentration was  $60\text{ mg L}^{-1}$ , and the initial pH was adjusted to 6.96 using HCl and NaOH solutions.

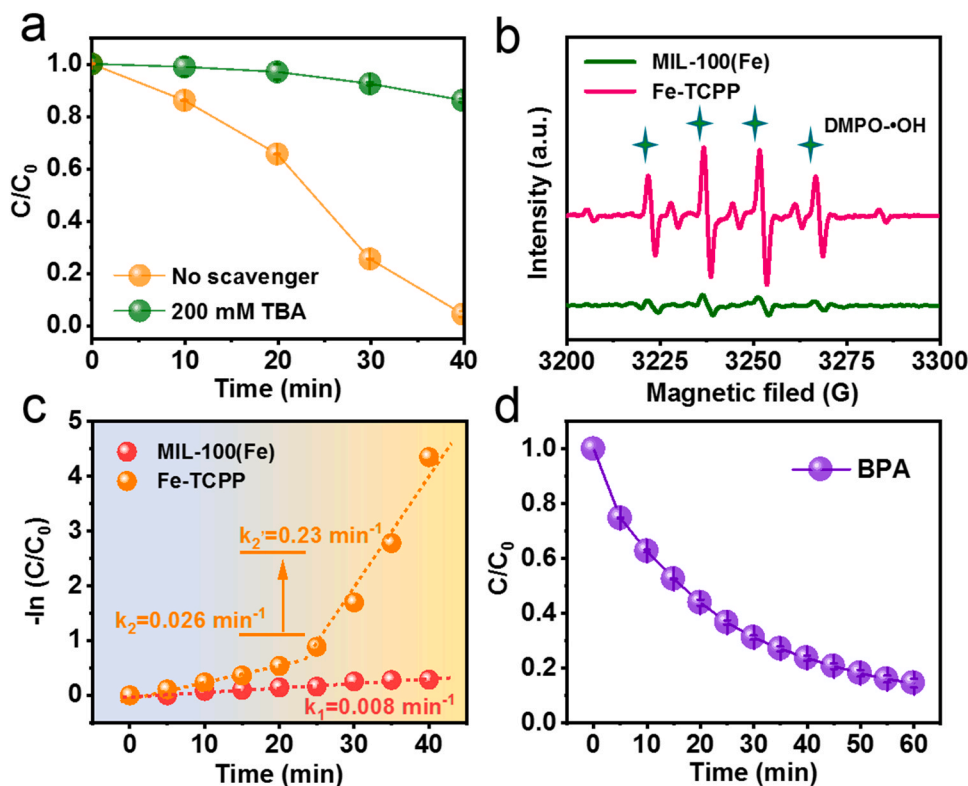


Fig. 5. Free radical quenching experiments on the CIP degradation (a); Measured DMPO-trapped EPR signals in Fe-TCPP and MIL-100(Fe) (b); Kinetic fitting of CIP degradation over Fe-TCPP and MIL-100(Fe) (c); Time profiles of BPA degradation efficiency over Fe-TCPP mediated photo-Fenton systems at  $25 \pm 2^\circ\text{C}$  under visible light irradiation (d). The initial concentrations of BPA and  $H_2O_2$  were  $10\text{ mg L}^{-1}$  and  $5\text{ mmol L}^{-1}$ , respectively. The catalyst concentration was  $60\text{ mg L}^{-1}$ , and the initial pH was adjusted to 7.02 using HCl and NaOH solutions.

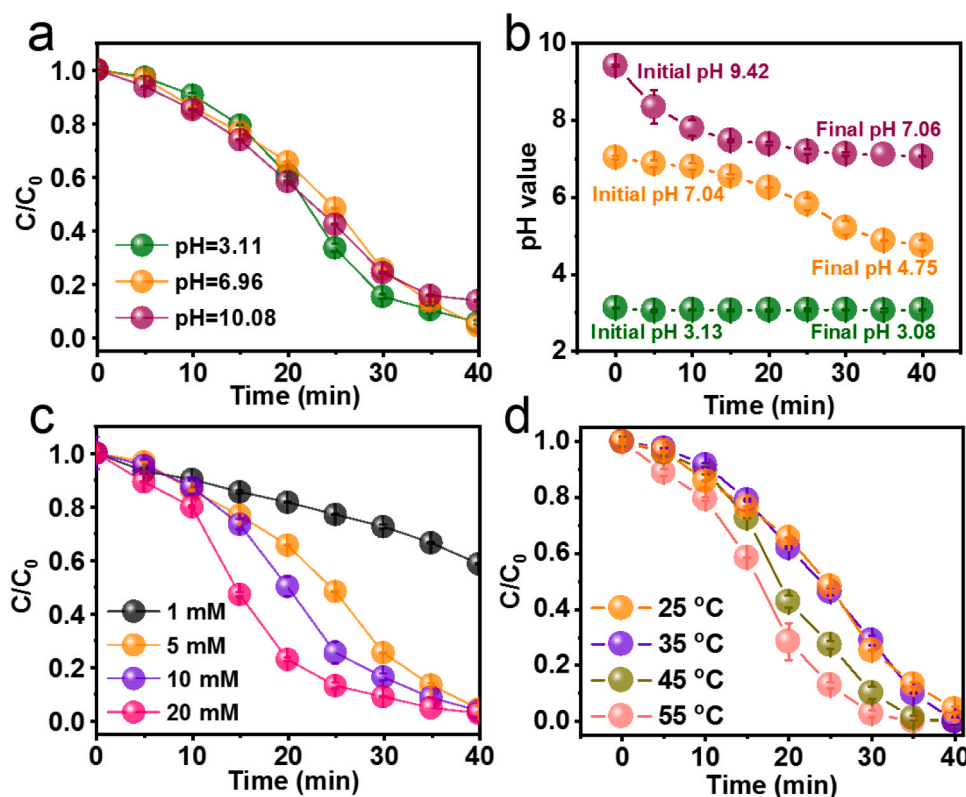


Fig. 6. Effect of pH difference on CIP degradation (a) and pH variation in the photo-Fenton process mediated by Fe-TCPP at different initial pH values (b); Effect of  $H_2O_2$  dosage (c) and reaction temperature (d) on CIP degradation in the photo-Fenton process driven by Fe-TCPP nanorods.

Fe(III) and TCPP  $p$ -cation radical were determined using a JEOL JES-FA200 under visible light radiation at 140 K.

### 2.5. Model construction and calculation methodology

The DFT calculations were performed using DMol<sup>3</sup> module implemented in the Materials Studio program for exploring the structural characteristics of Fe-TCPP in a micro-perspective [29]. Establishment of structural model of Fe-TCPP were conducted by referring to the previous report followed by configuration optimization [25]. Besides, molecular orbital (MO) properties of Fe-TCPP, including lowest unoccupied molecular orbital (LUMO) and highest occupied molecular orbital (HOMO), were calculated by generalized gradient approximation (GGA) PW91 exchange functional and double precision numerical basis set combined with  $p$ -orbital polarization function (DNP) [30]. The accuracy of energy convergence, maximum displacement and maximum gradient in the geometric optimization period were set as  $1 \times 10^{-5}$  Hartree,  $5 \times 10^{-3}$  Å and  $2 \times 10^{-3}$  Hartree/Å, respectively [31].

## 3. Results and discussion

### 3.1. Morphology and properties of Fe-TCPP

Fe-TCPP was successfully obtained as schemed in Fig. 1a [23]. Briefly, the  $Fe_3O(COO)_6$  clusters were formed at first by the coordination effect between  $Fe^{3+}$  and carboxyl groups (COOH) from TCPP ligands, which structured a pyramidal skeleton in the  $xy$  plane and inherently pillared by TCPP linkers to afford a three-dimensional (3D) framework (Fig. 1a, inset). The SEM and FETEM images (Fig. 1b–e) reveal uniform nanorod-like Fe-TCPP structure with a length of  $2 \mu m$  and a width of 100 nm. The elemental mapping analyses (Fig. 1d) confirm the uniform distribution of iron species and other constituent elements. As displayed in Fig. 1f, the atomic force microscope (AFM) images verify relatively

smooth surface morphology of Fe-TCPP, with a thickness distribution between 50 and 100 nm (Fig. 1g–h). Moreover, the information of Fe-TCPP structure was identified according to XRD results. As indicated in Fig. 2a, there is no obvious difference by comparing with the simulated structure, pointing to the consistency between Fe-TCPP structure and the simulated one (Fig. S1), in which the imperfect crystallinity could be due to the influence of surfactants [32–34].

On the other hand, the high resolution XPS spectra of Fe 2p in Fe-TCPP (Fig. 2b) feature three peaks located at 725.06, 714.32 and 711.35 eV, which are characteristic signals of Fe(III)-O species [35,36]. In addition, the evident signals at 1600 G and 3500 G in the EPR spectra (Fig. 2c) also signify the existence of Fe(III) according to the previous report [37]. Noteworthy, it is generally acknowledged that there were two potential Lewis bases sites including carboxyl (COOH) and unsaturated N sites in the center of TCPP structure that could form chemical bond with dissociative  $Fe^{3+}$  based on the Lewis acid-base theory [16]. The result of the high resolution XPS spectra of Fe 2p has indicated the formation of chemical bond between dissociative  $Fe^{3+}$  and COOH within TCPP molecule. Moreover, the fresh peaks in the Raman spectrum located at 204, 433, 706 and 768  $cm^{-1}$  were verified to belong to Fe-O species compared to the pristine TCPP (Fig. S2) [38,39]. Meanwhile, as clearly indicated in the Fourier transform infrared (FT-IR) spectra (Fig. 2d), the C-OH ( $1230 \text{ cm}^{-1}$ ) and C=O ( $1740 \text{ cm}^{-1}$ ) vibrations belonging to COOH are largely weakened when compared with that of TCPP molecule, also suggesting the successful coordination between dissociative  $Fe^{3+}$  and COOH within TCPP molecule. In addition, the ratio of TCPP and Fe is calculated to be 1:2, and the bond length of the Fe-O is about 1.89 Å based on density functional theory (DFT) calculations, which is in line with the results of previously reported octahedral iron(III)-hydroxide complexes (1.84–1.93 Å) [40].

Besides, results of the XPS spectra of N 1s show that both Fe-TCPP and TCPP molecules share identical peak positions, which indicates that dissociative  $Fe^{3+}$  did not interact with unsaturated N sites within

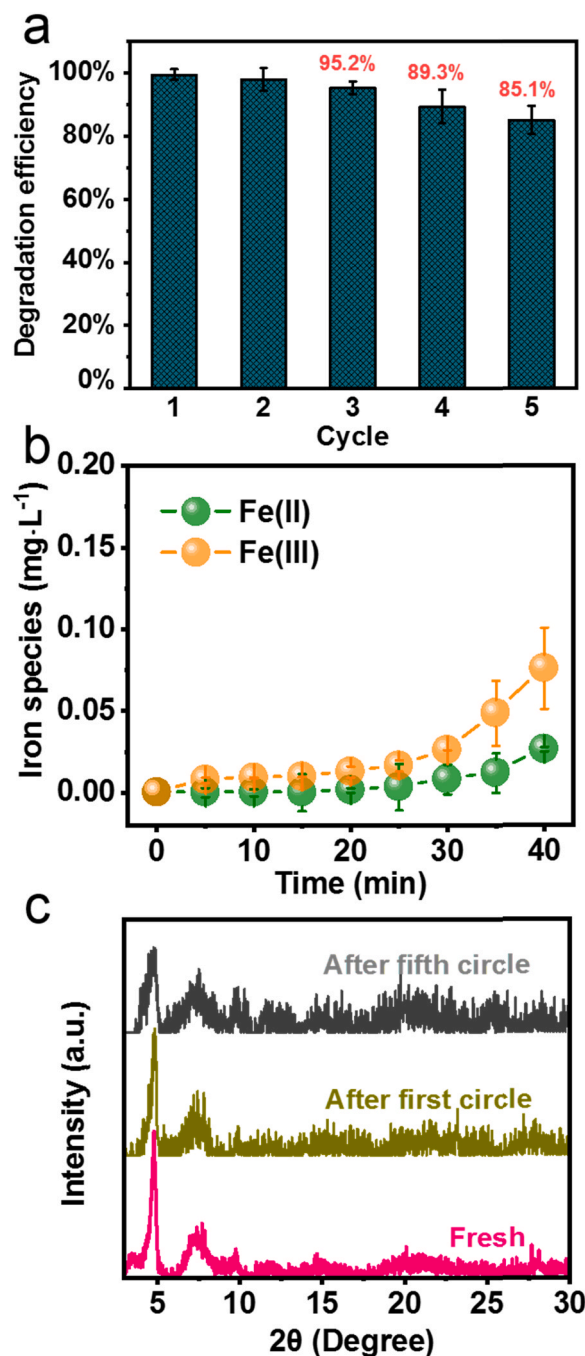


**Fig. 7.** Cycle test of CIP elimination (a) and concentration of iron species (b) in the photo-Fenton process mediated by Fe-TCPP; XRD pattern of the Fe-TCPP after reaction (c). The initial concentrations of CIP and H<sub>2</sub>O<sub>2</sub> were 25 mg L<sup>-1</sup> and 5 mmol L<sup>-1</sup>, respectively. The catalyst concentration was 60 mg L<sup>-1</sup>, and the initial pH was adjusted to 6.96 using HCl and NaOH solutions.

TCPP (Fig. 3a and b) [41]. The above conclusion was further confirmed through the result of UV-Vis spectra of Fe-TCPP/ethanol dispersion, where Fe-TCPP retains the specific quintuple peaks that are assigned to TCPP (Fig. 3c) [34]. In a word, dissociative Fe<sup>3+</sup> selectively bond with COOH instead of unsaturated N site in TCPP, where the main reason should be attributed to the difference of coordination ability between dissociative Fe<sup>3+</sup> and different Lewis bases [42]. Taking together, it is deduced that iron species only existed in the Fe<sub>3</sub>O(COO)<sub>6</sub> clusters in trivalent form, which would be the active site of Fe-TCPP for the decomposition of H<sub>2</sub>O<sub>2</sub> to •OH in the photo-Fenton system. In addition, the content of iron species in fresh Fe-TCPP (Table S1) determined by

inductively plasma atomic emission spectrometry (ICP-AES) was 11.50%, in close proximity to that of simulated structure (11.33%) (Fig. S1).

### 3.2. Photo-Fenton experiment evaluation

Having ascertained the structural and morphological identities of Fe-TCPP, we further evaluated its performance on CIP degradation at a neutral pH under visible light irradiation. The control experiments (Figs. 4a and S3a) with no detectable CIP concentration change highlights the important roles of both photocatalyst and H<sub>2</sub>O<sub>2</sub> as well as visible light irradiation. Typically, the pristine photocatalytic process with absence of H<sub>2</sub>O<sub>2</sub> results in weak CIP degradation efficiency, ascribing to the limited oxidation capacity of photogenerated holes (purple curves in Fig. 4a). Furthermore, the individual contribution of either Fe<sub>3</sub>O(COO)<sub>6</sub> or TCPP only accounts for negligible proportion to remove CIP (Fig. 4b), which could be interpreted as a result of sluggish charge separation or poor ability of photogenerated electrons to activate H<sub>2</sub>O<sub>2</sub> and produce •OH, respectively. Here, MIL-100(Fe) with the same Fe<sub>3</sub>O(COO)<sub>6</sub> clusters (Fig. 4c) was also employed to evaluate the importance of ligands in Fe-TCPP structure to initiate the photo-Fenton process [10]. Meanwhile, its content of iron species were determined to be 25.73% by ICP-AES, which was 2.2 times higher than that of Fe-TCPP (11.50%). Furthermore, the specific surface area of MIL-100 (Fe) is about 1110–1189 m<sup>2</sup> g<sup>-1</sup> according to literature reports [10,43], which is much higher than the value of Fe-TCPP (33.85 m<sup>2</sup> g<sup>-1</sup>) in Fig. S3b. Accordingly, MIL-100(Fe) had an obvious adsorption capacity of 38% for CIP under dark conditions and gradually plateaued after 40 min, as clearly shown in Fig. 4d. However, subsequent visible light irradiation only contributed to a low CIP degradation efficiency of 15% (Fig. 4b), in line with a previous report [44]. This is presumably ascribed to the single excitation process of Fe<sub>3</sub>O(COO)<sub>6</sub> cluster in MIL-100(Fe) with low-efficiency charge separation that gives rise to sluggish Fe(III)/Fe(II) transformation.

In sharp contrast, Fe-TCPP features encouraging CIP degradation effect in the photo-Fenton reaction (Fig. 4a, orange curve), as evidenced by the complete degradation of CIP in 40 min under identical conditions. Free radical quenching experiments were further conducted to identify ROS in the system, where excessive tert-butyl alcohol serves as the scavenger since it specifically keeps a high reactivity with •OH [4]. As expected, the CIP degradation efficiency was substantially lowered after the addition of 200 mM tert-butyl alcohol (Fig. 5a), indicating the importance of •OH as predominant ROS in this system. Moreover, the DMPO-trapped EPR results manifest stronger quadruple signals (relative intensity is 1:2:2:1) that belong to DMPO-•OH adduct (Fig. 5b), which demonstrates that the superior CIP degradation efficiency of Fe-TCPP in photo-Fenton process was achieved by the production of more •OH compared to MIL-100(Fe) [45]. Meanwhile, the additional signals in the EPR spectrum of DMPO-•OH adduct were detected in Fig. 5b, pertaining to aminoxyl radical ([R<sub>2</sub>N-O] [R<sub>2</sub>N<sup>+</sup>-O<sup>-</sup>]) generated by oxidation of the amine functionality from CIP [45,46], as confirmed by the results of EPR in Fig. S4. Besides, the signal of DMPO-O<sub>2</sub><sup>•</sup> was also captured as shown in Fig. S5, which is attributed to the reaction between Fe(III) and H<sub>2</sub>O<sub>2</sub> [47]. It is of particular interest that the pseudo-first-order reaction kinetic fitting results reveal that the rate constant (k) for CIP degradation was self-enhanced dramatically after 20 min (Fig. 5c), which is primarily due to the incremental concentration of accumulated •OH to 56.3 μM within 40 min, as confirmed by the results of benzoate probe experiments (Fig. S6a) and the EPR spectra (Fig. S6b) [1]. The observed k values for Fe-TCPP are 0.026 and 0.23 min<sup>-1</sup> for the first half and second half of the process, which are 3 and 29 times higher than that of MIL-100(Fe) (0.008 min<sup>-1</sup>), respectively. Moreover, the k value of 0.23 min<sup>-1</sup> for Fe-TCPP significantly surpass the performance of state-of-the-art photocatalyst materials listed in Table S2 except for U-g-PAO/Fe, especially for the MOFs modified by semiconductors or co-catalysts. In addition to CIP, the Fe-TCPP mediated photo-Fenton



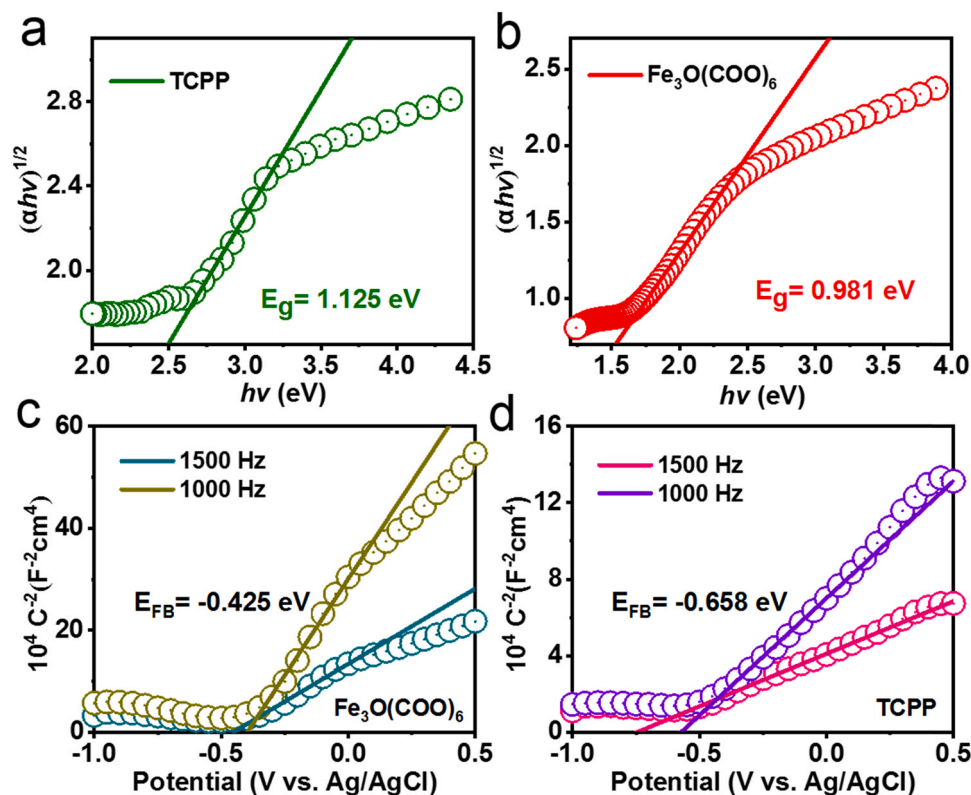


Fig. 8. Plot of the  $(\alpha hv)^{1/2}$  versus  $h\nu$  for TCPP (a) and  $\text{Fe}_3\text{O}(\text{COO})_6$  (b); Typical Mott-Schottky plots of  $\text{Fe}_3\text{O}(\text{COO})_6$  (c) and TCPP (d).

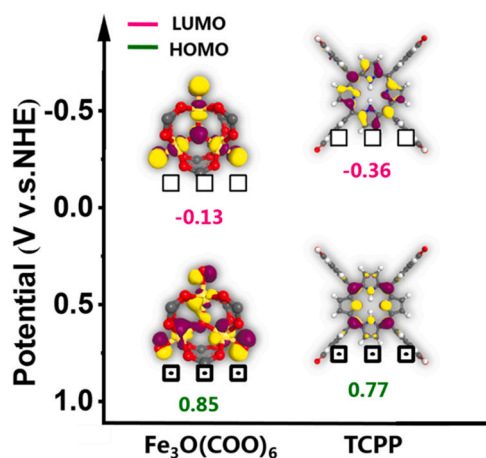


Fig. 9. Schematic diagram of energy band distribution of TCPP and  $\text{Fe}_3\text{O}(\text{COO})_6$ .

system has been proven to keep the universality in the degradation of other refractory organic pollutants, such as bisphenol A (BPA), as displayed in Fig. 5d.

Besides, the photo-Fenton system based on Fe-TCPP was qualified to maintain a high reactivity in pH range of 3–10 (Fig. 6a). Furthermore, the pH variation in the system with different initial pHs was explored, as shown in Fig. 6b. Being different from the initially acidic environment which showed not obvious changes of pH values, the system was found to be acidified with prolonging reaction time in initially neutral and alkaline pH environments, which is consistent with the results reported by Guo et al. [48]. The possible reasons are summarized into the following points including: (i) the  $\text{Fe}_3\text{O}(\text{COO})_6$  cluster in Fe-TCPP could coordinate with  $\text{H}_2\text{O}$  accompany by  $\text{H}^+$  release [49]; (ii) the  $\text{OH}^-$  was consumed due to the hydrolysis process of the partially released  $\text{Fe}^{3+}$

[48]; (iii) small molecular organic acids were produced during the degradation of CIP [50]. Moreover, the degradation rate of CIP was obviously improved as the reaction temperature improved from 25 to 55 °C and  $\text{H}_2\text{O}_2$  concentration increased from 1 to 20 mM in the system (Fig. 6c and d), respectively. Interestingly, we also prove that this LCCT excitations strategy is also feasible in photo-Fenton-like system mediated with copper-based MOFs (Cu-TCPP), as shown in Fig. S7.

It is well known that the reusability and stability of materials are critical to the process of removing pollutants from actual water bodies. As expected, the removal efficiency of CIP still maintained about 85% after five cycles (Fig. 7a), which was acceptable compared to reported results, indicating Fe-TCPP hold good reusability. Meanwhile, the dissolution amount of Fe species in the system was 0.1 mg  $\text{L}^{-1}$  after 40 min, including 0.075 mg  $\text{L}^{-1}$  of Fe(III) and 0.025 mg  $\text{L}^{-1}$  of Fe(II) as displayed in Fig. 7b, which was far lower than the environmental standard value (2.0 mg  $\text{L}^{-1}$ ) [7]. More importantly, the results of SEM and XRD indicate that the morphology and structure of Fe-TCPP did not change significantly after the first and fifth cycle experiments (Figs. S8 and Fig. 7c) compared to the fresh one, respectively. In summary, the results manifest that Fe-TCPP has a good stability under water treatment process. Besides, the reasons for the decrease in the efficiency of the catalyst in the cycle experiment might be mainly attributed to the following two points according to the results of SEM (Fig. S9). Firstly, the materials after reaction tend to agglomerate due to the larger surface energy of nanomaterials, which is not conducive to contact with pollutants [15]. Moreover, the degradation products of CIP would adhere to the surface of the material (yellow dashed box in Fig. S9d), which blocked the exposed of active sites and resulted in hindered hydrogen peroxide activation process [51].

### 3.3. Identification of LCCT excitations within Fe-TCPP

In order to verify the feasibility of LCCT excitations between  $\text{Fe}_3\text{O}(\text{COO})_6$  clusters and TCPP ligands in Fe-TCPP, the energy band

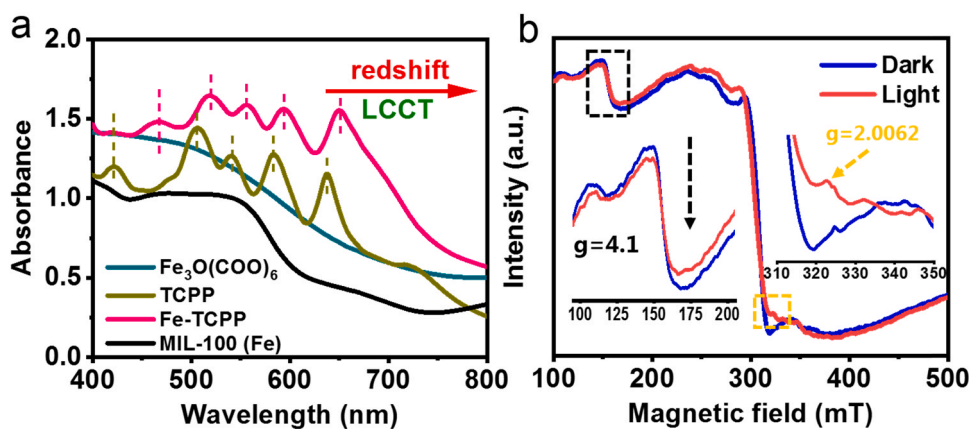


Fig. 10. UV-vis absorption spectra of prepared photocatalysts (a); Low-temperature EPR spectra of Fe-TCPP before and after irradiation for 2 min at 140 K (b).

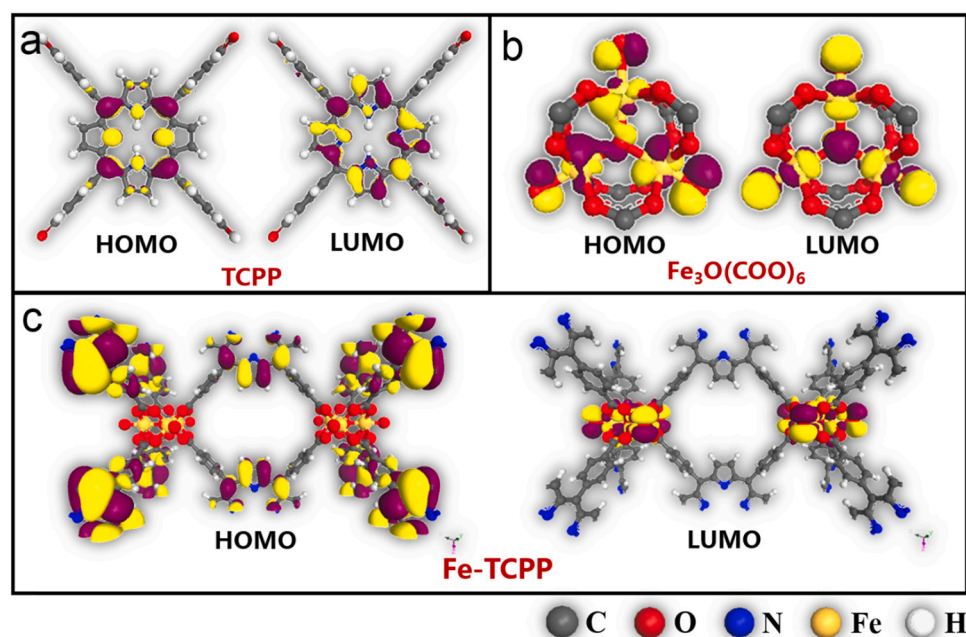


Fig. 11. Simulated molecular orbital diagrams of TCPP (a),  $\text{Fe}_3\text{O}(\text{COO})_6$  (b) and Fe-TCPP nanorods (c).

distribution of  $\text{Fe}_3\text{O}(\text{COO})_6$  and TCPP have been carefully studied. Firstly, the band gap ( $E_g$ ) of the photocatalysts were measured according to the Tauc plot method [17]. As shown in Fig. 8a and b, both TCPP and  $\text{Fe}_3\text{O}(\text{COO})_6$  displayed much narrower band gaps of 1.13 and 0.98 eV, respectively. Afterwards, the Mott-Schottky measurements reveal their feature of typical n-type semiconductor since the positive slope for the linear plots as displayed in Fig. 8c and d [17]. Meanwhile, the flat band potential ( $E_{fb}$ ) of TCPP and  $\text{Fe}_3\text{O}(\text{COO})_6$  were also determined were  $-0.43$  V and  $-0.66$  V vs. Ag/AgCl electrode (i.e., 0.17 and  $-0.06$  V vs. NHE, pH = 6.8), respectively [21]. Furthermore, the energy level of LUMO of  $\text{Fe}_3\text{O}(\text{COO})_6$  and TCPP could be identified as  $-0.13$  V and  $-0.36$  V vs. NHE from the approximate process that the LUMO of typical n-type semiconductor is about 0.3 V below  $E_{fb}$  [52]. Accordingly, the LUMO/HOMO of  $\text{Fe}_3\text{O}(\text{COO})_6$  and TCPP can be calculated by Eq. (4), which are  $-0.13$  V/0.85 V and  $-0.36$  V/0.77 V, respectively [21].

$$E_g = \text{HOMO} - \text{LUMO} \quad (4)$$

In brief, the overall energy band structure diagrams can be drawn based on the above results (Fig. 9). Since the energy level of LUMO of  $\text{Fe}_3\text{O}(\text{COO})_6$  is lower than that of TCPP, electron transition from the HOMO of the TCPP ligand to the LUMO of the  $\text{Fe}_3\text{O}(\text{COO})_6$  cluster is

more likely to occur upon excitation, which well supports the theoretical feasibility of LCCT excitations that occurred within Fe-TCPP [53].

Besides, optical properties of the component within Fe-TCPP were explored by the UV-visible absorption spectra for identification of LCCT excitations. As shown in Fig. 10a, TCPP shows strong absorption within the visible light wavelength range as a result of its structural similarity to photosynthetic chromophores (yellow curve) [24]. The typical absorption is also evidenced in Fe-TCPP (pink curve), which displays a higher absorption intensity toward visible light along with a significant red shift, declaring the LCCT excitations exist between TCPP ligands and  $\text{Fe}_3\text{O}(\text{COO})_6$  clusters [18,53]. Although MIL-100(Fe) is capable of absorbing visible light by the  $\text{Fe}_3\text{O}(\text{COO})_6$  cluster, it is found that the absorption intensity was obviously lower than that of the Fe-TCPP (pink curve), which is probably ascribed to no appearance of LCCT excitations since the benzenetricarboxylic acid as the ligand is of no photosensitivity. More importantly, photoelectron transfer pathway was further unveiled by in-situ EPR at 140 K under visible light irradiation. As displayed in Fig. 10b, a new ESR signal corresponding to TCPP p-cation radical at  $g = 2.0062$  emerged in Fe-TCPP. Meanwhile, the EPR signal centered at  $g = 4.10$  corresponding to high-spin Fe(III) decreased rapidly after light illumination for 2 min, signifying photoelectron derived from

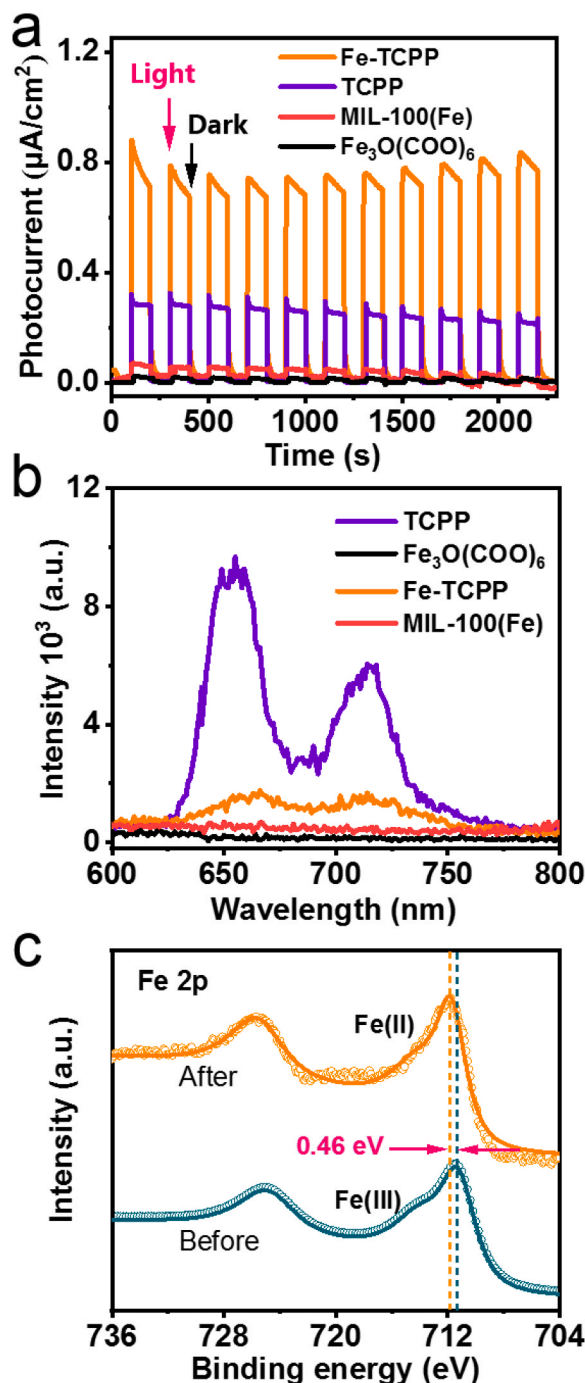


Fig. 12. Transient photocurrent response curves of different catalysts (a); Steady-state fluorescence spectrum of different catalysts (b); XPS spectra of Fe-TCPP photocatalyst before and after visible light illumination (c).

TCPP transfer to  $\text{Fe}_3\text{O}(\text{COO})_6$  clusters, where Fe(III)/Fe(II) transformation was initiated [21,54,55].

Finally, the orbital distribution characteristics of Fe-TCPP were evaluated by DFT calculations to further corroborating the above results. As depicted in Fig. 11a and b, nearly identical HOMO and LUMO distributions appear in both individual TCPP and  $\text{Fe}_3\text{O}(\text{COO})_6$  molecules, which proves the characterization of the energy band structure, that is, too narrow band gap would increase the recombination rate of photogenerated carriers. In contrast, it clearly shows that HOMO and LUMO were composed of TCPP ligands and  $\text{Fe}_3\text{O}(\text{COO})_6$  clusters within Fe-TCPP structure, respectively, which is more likely to realize LCCT

excitations accompany space separation of photocarriers because of the suitable orbital distribution difference (Fig. 11c) [52]. In summary, LCCT excitations as the main source of photoactivities were successfully introduced into Fe-TCPP by coupling TCPP ligands with  $\text{Fe}_3\text{O}(\text{COO})_6$  clusters in this study.

### 3.4. Possible mechanisms of boosting CIP degradation over Fe-TCPP

The separation and recombination efficiencies of the photocarriers within the photocatalysts under visible light irradiation were investigated by using transient photocurrent measurement and steady-state fluorescence spectrum. As depicted in Fig. 12a and b, for  $\text{Fe}_3\text{O}(\text{COO})_6$  (black curve) and MIL-100(Fe) (red curve), the weak photocurrent signal and minimal fluorescence intensity indicates the low carrier separation efficiency, where the energy of the excited state might be emitted from the system in a non-radiative manner [56]. Besides, TCPP molecule displays distinct photocurrent signal together with intense fluorescence (Fig. 12a and b, purple curve), this is attributed to the fact that the excited state quickly returns to the ground state and releases the energy in the form of fluorescence [57]. As expected, the highest photocurrent signal was detected in Fe-TCPP (Fig. 12a, orange curve), declaring that the separation process of photogenerated carrier benefit from LCCT excitations is highly efficient, meanwhile, recombination process of photogenerated carrier was suppressed according to the weak steady-state fluorescence intensity (Fig. 12b, orange curve) [23]. As a result, the accumulated photogenerated electrons would participate in the Fe(III)/Fe(II) cycle [58], which has been confirmed in the Section 3.3 based on the results of the low-temperature EPR (Fig. 10b). Besides, XPS spectra of Fe-TCPP samples before and after visible light irradiation were also collected to verify occurrence of Fe(III)/Fe(II) cycle driven by photoelectron result from LCCT excitations. An evident shift about 0.46 eV corresponding to Fe 2p peak was detected after photoexcitation (Fig. 12c), which could be attributed to Fe(II) species generation. Furthermore, The Fitting of Fe 2p region shows coexisting Fe(II)/(III) valency with approximately 5.8% Fe(II) and 94.2% Fe(III) in Fe-TCPP under visible light irradiation in Fig. S10 [59]. Thus, these results demonstrate that the  $(\text{III})\text{Fe}_3\text{O}(\text{COO})_6$  clusters was able to translate  $(\text{II})\text{Fe}_3\text{O}(\text{COO})_6$  by accepting the photoelectrons, consistent with previous report [54]. Overall, the combined findings unambiguously verify that the existence of LCCT excitations in Fe-TCPP not only improved the photogenerated carrier separation efficiency but also suppressed their recombination, where accumulated photogenerated electron engaged in Fe(III)/Fe(II) transformation.

It is known that the essence of the photo-Fenton process was grounded on generation of charge-separated-states species following charge separation [48,60]. Direct evidence involved in the production of charge-separated-states species, that is  $(\text{II})\text{Fe}_3\text{O}(\text{COO})_6$ , following the photoelectron-mediate Fe(III)/Fe(II) transformation after LCCT excitations in the Fe-TCPP, would be highly important for unveiling the relevant mechanisms behind improved performance [20]. Here, NTA spectra were utilized to further track the real-time charge separation process of these materials for exploring generation of charge-separated-states species [26,61]. For pristine TCPP, there is no obvious positive-value absorption signal, but it is accompanied by a strong fluorescence signal located at 650 and 730 nm after light irradiation (Fig. S11a), which manifested no charge-separation-state species were produced from TCPP after photoexcitation [26]. However, a positive-value absorption signal was observed at 730 nm in the  $\text{Fe}_3\text{O}(\text{COO})_6$  NTA spectra (Fig. 13a, dotted box), and similar spectral features signal were also discovered at 840 nm in the NTA spectra of both MIL-100(Fe) and Fe-TCPP (Fig. 13b and c, dotted box). It can be inferred that the signal of charge-separated-states species belong to  $(\text{II})\text{Fe}_3\text{O}(\text{COO})_6$  structure since all three photocatalytic materials share a common  $(\text{III})\text{Fe}_3\text{O}(\text{COO})_6$  structure. Additionally, the average apparent lifetime of  $(\text{II})\text{Fe}_3\text{O}(\text{COO})_6$  species in Fe-TCPP was  $52 \pm 0.4$  ns, lower than that of MIL-100(Fe) ( $151 \pm 3$  ns), at a catalyst dosage of  $60 \text{ mg L}^{-1}$ .



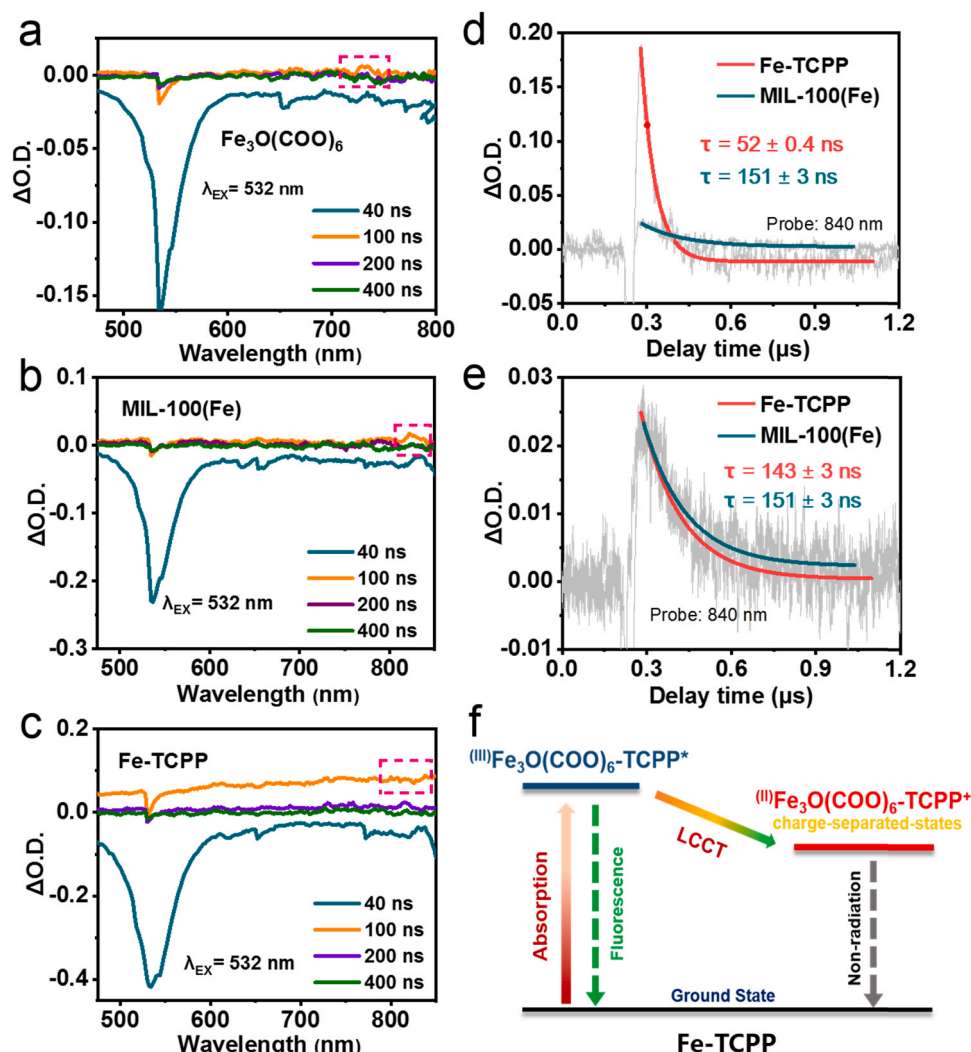


**Fig. 13.** NTA spectra excited by 532 nm laser pulse for  $\text{Fe}_3\text{O}(\text{COO})_6$  (a), MIL-100(Fe) (b) and Fe-TCPP (c) at room temperature; The NTA kinetics at 840 nm of Fe-TCPP and MIL-100(Fe) (d); The NTA kinetics at 840 nm of 50 times diluted suspensions of Fe-TCPP (e); Simplified Jablonski diagram for charge transfer processes between cluster and ligand within Fe-TCPP (f).

(Fig. 13d), ascribing to the well-known self-quenching effect [62]. However, the average apparent lifetime of  $(\text{III})\text{Fe}_3\text{O}(\text{COO})_6$  species in Fe-TCPP and MIL-100(Fe) became similar, when the population of  $(\text{III})\text{Fe}_3\text{O}(\text{COO})_6$  species were deliberately diluted to the same concentration (Figs. 13e and S11b). This further affirms that the charge-separated-states species generated inside Fe-TCPP were as same as that of MIL-100(Fe) after photoexcitation. On the other hand, the single exponential fitting results also manifest that the population of  $(\text{III})\text{Fe}_3\text{O}(\text{COO})_6$  species excited within Fe-TCPP was about 8 times of MIL-100(Fe) under the same time and photocatalyst concentration (Fig. 13d), emphasizing that the Fe(III)/Fe(II) transformation are accelerated on account of more photoelectron participation originate from LCCT excitations. Hence, the mechanism of the transition and transfer of the photogenerated electrons in the Fe-TCPP under visible light irradiation is depicted in Fig. 13f. That is, the ground state of Fe-TCPP ( $(\text{III})\text{Fe}_3\text{O}(\text{COO})_6\text{-TCPP}$ ) reaches the higher-lying excited state ( $(\text{III})\text{Fe}_3\text{O}(\text{COO})_6\text{-TCPP}^*$ ) after excitation, and then transfer to lower-lying charge-separated-states [ $(\text{III})\text{Fe}_3\text{O}(\text{COO})_6\text{-TCPP}^+$ ] though LCCT excitations, which finally participate in the activation of  $\text{H}_2\text{O}_2$  to  $\cdot\text{OH}$ .

To sum up, the improvement of CIP degradation performance mediated by Fe-TCPP under photo-Fenton reaction could be attributed to the mechanism shown in Fig. 14 below. Apart from the subordinate

single excitation process of the  $\text{Fe}_3\text{O}(\text{COO})_6$  clusters within Fe-TCPP. The photogenerated electrons stem from excited TCPP ligands were quickly transfer to the  $\text{Fe}_3\text{O}(\text{COO})_6$  cluster through LCCT excitations and further accelerated Fe(III)/Fe(II) transformation under visible light irradiation, which principally contributes to the activation of  $\text{H}_2\text{O}_2$  to plentiful  $\cdot\text{OH}$  for rapid CIP degradation.

#### 4. Conclusion

This study for the first time demonstrates that the introduction of LCCT excitations is an effective strategy to boost photo-Fenton performance via accelerating the Fe(III)/Fe(II) transformation. The developed Fe-TCPP nanorods with the  $k$  value of  $0.23 \text{ min}^{-1}$  toward antibiotic elimination was approximately 29 times that of MIL-100(Fe) ( $0.008 \text{ min}^{-1}$ ), and kept no obvious performance changes at a wide pH range of 3–10. Meanwhile, the overwhelming performance advantage was achieved compared to the state-of-the-art photocatalysts under the visible light induced photo-Fenton system. It is revealed that LCCT excitations occurred between porphyrin ligands and iron-oxo cluster within Fe-TCPP nanorods, contributing to abundant photogenerated electrons that dramatically accelerate dull Fe(III)/Fe(II) transformation. As such, the resulting charge-separated-states species with high population could activate  $\text{H}_2\text{O}_2$  to generate more  $\cdot\text{OH}$  that is responsible for

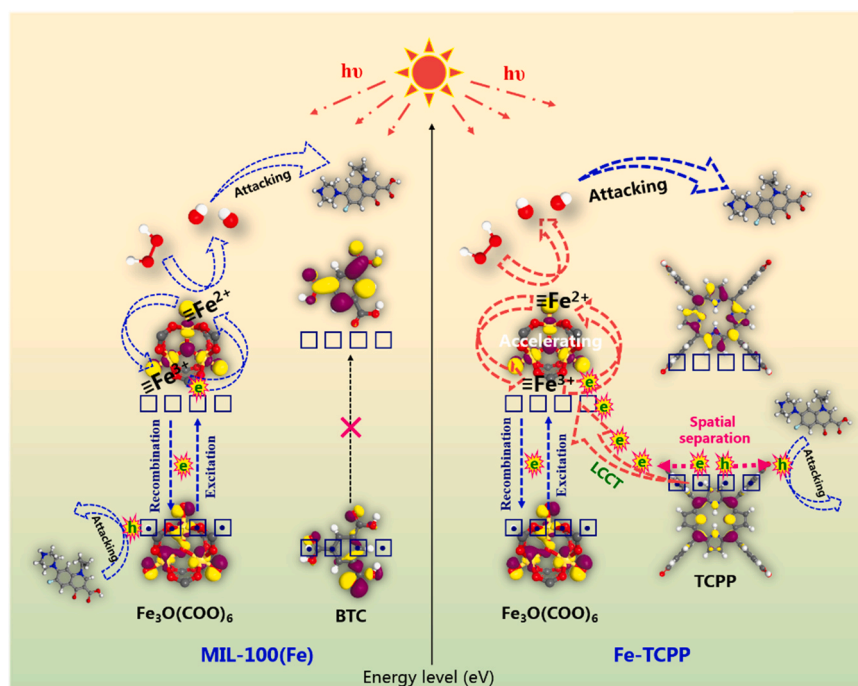


Fig. 14. Proposed mechanism for highly efficient CIP removal over Fe-TCPP under photo-Fenton process based on LCCT excitations pathway.

highly efficient CIP degradation under photo-Fenton process. Additionally, the introduction of LCCT excitations is also effective for the Fenton-like system induced by copper-based MOFs under visible light. Our work may provide a new strategy to manipulate photo-Fenton or photo-Fenton-like reactions mediated by different types of MOFs, which would be useful for the application of MOFs in the pollutant elimination.

#### CRediT authorship contribution statement

**Wen-Qiang Li:** Investigation, Methodology, Data curation, Writing – original draft. **Yi-Xuan Wang:** Writing – review & editing, Data curation, **Jia-Qi Chen:** Data curation, **Nan-Nan Hou:** Writing – review & editing, Supervision. **Yuan-Ming Li:** Methodology, Data curation. **Xiao-Cheng Liu:** Methodology, Reviewing. **Rong-Rong Ding:** Data curation. **Guan-Nan Zhou:** Data curation. **Qi Li:** Visualization. **Xiao-Guo Zhou:** Visualization. **Yang Mu:** Data curation, Writing – review & editing, Supervision.

#### Declaration of Competing Interest

The authors declare that they have no known competing financial interests or personal relationships that could have appeared to influence the work reported in this paper.

#### Acknowledgements

The authors appreciate the financial support provided by the National Natural Science Foundation of China (U19A20108, 52025101, 51878637 and 51821006).

#### Appendix A. Supporting information

Supplementary data associated with this article can be found in the online version at [doi:10.1016/j.apcatb.2021.120882](https://doi.org/10.1016/j.apcatb.2021.120882).

#### References

- [1] F. Xiao, X.Q. Shen, H.Y. Zhao, Y. Chen, C. Fang, R. Xiao, W.H. Chu, G.H. Zhao, In situ-formed PdFe nanoalloy and carbon defects in cathode for synergic reduction-

- oxidation of chlorinated pollutants in electro-Fenton process, *Environ. Sci. Technol.* 54 (2020) 4564–4572.
- [2] R.L. Liu, Y.M. Xu, B.L. Chen, Self-assembled nano-FeO(OH)/reduced graphene oxide aerogel as a reusable catalyst for photo-Fenton degradation of phenolic organics, *Environ. Sci. Technol.* 52 (2018) 7043–7053.
- [3] H.C. Lan, F. Wang, M. Lan, X.Q. An, H.J. Liu, J.H. Qu, Hydrogen-bond-mediated self-assembly of carbon-nitride-based photo-Fenton-like membranes for wastewater treatment, *Environ. Sci. Technol.* 53 (2019) 6981–6988.
- [4] J.J. Hu, S. Wang, J.Q. Yu, W.K. Nie, J. Sun, S.B. Wang, Duet Fe<sub>3</sub>C and FeN<sub>x</sub> sites for H<sub>2</sub>O<sub>2</sub> generation and activation toward enhanced electro-Fenton performance in wastewater treatment, *Environ. Sci. Technol.* 55 (2021) 1260–1269.
- [5] L. Demarchis, M. Minella, R. Nistico, V. Maurino, C. Minero, D. Vione, Photo-Fenton reaction in the presence of morphologically controlled hematite as iron source, *J. Photochem. Photobiol. A* 307 (2015) 99–107.
- [6] M. Ahmad, S. Chen, F. Ye, X. Quan, S. Afzal, H.T. Yu, X.Y. Zhao, Efficient photo-Fenton activity in mesoporous MIL-100(Fe) decorated with ZnO nanosphere for pollutants degradation, *Appl. Catal. B Environ.* 245 (2019) 428–438.
- [7] M. Ahmad, X. Quan, S. Chen, H.T. Yu, Tuning Lewis acidity of MIL-88B-Fe with mix-valence coordinatively unsaturated iron centers on ultrathin Ti<sub>3</sub>C<sub>2</sub> nanosheets for efficient photoFenton reaction, *Appl. Catal. B Environ.* 264 (2020), 118534.
- [8] D.K. Wang, M.T. Wang, Z.H. Li, Fe-based metal-organic frameworks for highly selective photocatalytic benzene hydroxylation to phenol, *ACS Catal.* 5 (2015) 6852–6857.
- [9] M. Cheng, C. Lai, Y. Liu, G.M. Zeng, D.L. Huang, C. Zhang, L. Qin, L. Hu, C.Y. Zhou, W.P. Xiong, Metal-organic frameworks for highly efficient heterogeneous Fenton-like catalysis, *Coord. Chem. Rev.* 368 (2018) 80–92.
- [10] X. He, H. Fang, D.J. Gosztola, Z. Jiang, P. Jena, W.N. Wang, Mechanistic insight into photocatalytic pathways of MIL-100(Fe)/TiO<sub>2</sub> composites, *ACS Appl. Mater. Interfaces* 11 (2019) 12516–12524.
- [11] P. Jin, L. Wang, S.H. Duan, J.W. Huang, H.D. She, Q.Z. Wang, T.C. An, Accelerated Fenton-like kinetics by visible-lightdriven catalysis over iron(III) porphyrin functionalized zirconium MOF: effective promotion on the degradation of organic contaminants, *Environ. Sci. Nano* 6 (2019) 2652–2661.
- [12] D. Sheberla, J.C. Bachman, J.S. Elias, C.J. Sun, Y.H. Shao, M. Dinca, Conductive MOF electrodes for stable supercapacitors with high areal capacitance, *Nat. Mater.* 16 (2017) 220–224.
- [13] M.K. Naguib, V. Presser, J. Lu, J.J. Niu, M. Heon, L. Hultman, Y. Gogotsi, M. W. Barsoum, Two-dimensional nanocrystals produced by exfoliation of Ti<sub>3</sub>AlC<sub>2</sub>, *Adv. Mater.* 23 (2011) 4248–4253.
- [14] M.R. Lukatskaya, M. Ghidui, M.Q. Zhao, Y. Gogotsi, M.W. Barsoum, Conductive two-dimensional titaniumcarbide ‘clay’ with high volumetric capacitance, *Nature* 516 (2014) 78–81.
- [15] C.F. Zhang, L. McKeon, M.P. Kremer, S.H. Park, O. Ronan, A. Seral-Ascaso, S. Barwich, C.O. Coileain, N. McEvoy, H.C. Nerl, B. Anasori, J.N. Coleman, Y. Gogotsi, V. Nicolosi, Additive-free MXene inks and direct printing of micro-supercapacitors, *Nat. Commun.* 10 (2019) 1–9.
- [16] C. Zou, C.D. Wu, Functional porphyrinic metal-organic frameworks: crystal engineering and applications, *Dalton Trans.* 41 (2012) 3879–3888.

- [17] H.Q. Xu, J.H. Hu, D.K. Wang, Z.H. Li, Q. Zhang, Y. Luo, S.H. Yu, H.L. Jiang, Visible-light photoreduction of CO<sub>2</sub> in a metal-organic framework: Boosting electron-hole separation via electron trap states, *J. Am. Chem. Soc.* 137 (2015) 13440–13443.
- [18] T. Zhang, W.B. Lin, Metal-organic frameworks for artificial photosynthesis and photocatalysis, *Chem. Soc. Rev.* 43 (2014) 5982–5993.
- [19] L.G. agliardi, X.P. Wu, D.G. Truhlar, Cerium metal-organic framework for photocatalysis, *J. Am. Chem. Soc.* 140 (2018) 7904–7912.
- [20] B. Pattengale, S.Z. Yang, J. Ludwig, Z.Q. Huang, X.Y. Zhang, J. Huang, Exceptionally long-lived charge separated state in zeolitic imidazolate framework: implication for photocatalytic application, *J. Am. Chem. Soc.* 138 (2016) 8072–8075.
- [21] C.Y. Xu, H. Liu, D.D. Li, J.H. Su, H.L. Jiang, Direct evidence of charge separation in a metal-organic framework: efficient and selective photocatalytic oxidative coupling of amines via charge and energy transfer, *Chem. Sci.* 9 (2018) 3152–3158.
- [22] C.G. Silva, I. Luz, F.X.L.I. Xamena, A. Corma, H. Garcia, Water stable Zr-benzenedicarboxylate metal-organic frameworks as photocatalysts for hydrogen generation, *Chem. Eur. J.* 16 (2010) 11133–11138.
- [23] T. Liu, Q. Zuo, C.S. Chen, Y. Ji, X.Q. Gong, Y.Y. Mai, Y.F. Zhou, Ultrathin metal-organic framework nanosheets with ultrahigh loading of single Pt atoms for efficient visible-light-driven photocatalytic H<sub>2</sub> evolution, *Angew. Chem. Int. Ed.* 58 (2019) 10198–10203.
- [24] Z.J. Zhang, Y.F. Zhu, X.J. Chen, H.J. Zhang, J. Wang, A full-spectrum metal-free porphyrin supramolecular photocatalyst for dual functions of highly Efficient hydrogen and oxygen evolution, *Adv. Mater.* 31 (2019), 1806626.
- [25] K.C. Wang, D.W. Feng, T.F. Liu, J. Su, S. Yuan, Y.P. Chen, M. Bosch, X.D. Zou, H. C. Zhou, A series of highly stable mesoporous metalloporphyrin Fe-MOFs, *J. Am. Chem. Soc.* 136 (2014) 13983–13986.
- [26] M. Zhou, Y.X. Wei, Q.H. Zhou, X.G. Zhou, S.L. Liu, S. Zhang, B. Zhang, Triplet-triplet annihilation upconversion kinetics of C<sub>60</sub>-Bodipy dyads as organic triplet photosensitizers, *Phys. Chem. Chem. Phys.* 19 (2017) 22049–22060.
- [27] Q.H. Zhou, Y.X. Wei, X. Liu, L. Chen, X.G. Zhou, S.L. Liu, Photochemical reaction between 1,2-naphthoquinone and adenine in binary water-acetonitrile solutions, *Photochem. Photobiol.* 94 (2018) 61–68.
- [28] D.J. Greensmith, Ca analysis: an Excel based program for the analysis of intracellular calcium transients including multiple, simultaneous regression analysis, *Comput. Methods Prog. Biomed.* 113 (2014) 241–250.
- [29] X.C. Liu, C.S. He, Z.Y. Shen, W.Q. Li, N. Chen, J.S. Song, X.G. Zhou, Y. Mu, Mechanistic study of Fe(III) chelate reduction in a neutral electro-Fenton process, *Appl. Catal. B Environ.* 278 (2020), 119347.
- [30] J.P. Perdew, K. Burke, M. Ernzerhof, Generalized gradient approximation made simple, *Phys. Rev. Lett.* 77 (1996) 3865–3868.
- [31] X.C. Liu, W.Q. Li, Y.R. Wang, G.N. Zhou, Y.X. Wang, C.S. He, G.M. Wang, Y. Mu, Cathode-introduced atomic H\* for Fe(II)-complex regeneration to effective electro-Fenton process at a natural pH, *Environ. Sci. Technol.* 53 (2019) 6927–6936.
- [32] L.S. Sun, C.L. Wang, X.X. Wang, L.M. Wang, Morphology evolution and control of Mo-polydopamine coordination complex from 2D single nanopetal to hierarchical microflowers, *Small* 14 (2018), 1800090.
- [33] Y.X. Wang, M.T. Zhao, J.F. Ping, B. Chen, X.H. Cao, Y. Huang, C.L. Tan, Q.L. Ma, S. X. Wu, Y.F. Yu, Q.P. Lu, J.Z. Chen, W. Zhao, Y.B. Ying, H. Zhang, Bioinspired design of ultrathin 2D bimetallic metal-organic-framework nanosheets used as biomimetic enzymes, *Adv. Mater.* 28 (2016) 4149–4155.
- [34] M.T. Zhao, Y.X. Wang, Q.L. Ma, Y. Huang, X. Zhang, J.F. Ping, Z.C. Zhang, Q.P. Lu, Y.F. Yu, H. Xu, Y.L. Zhao, H. Zhang, Ultrathin 2D metal-organic framework nanosheets, *Adv. Mater.* 27 (2015) 7372–7378.
- [35] G.N. Zhou, C.S. He, Y.X. Wang, P.P. He, J. Liu, Y. Mu, L.S. Zhang, Aerobic removal of iodinated contrast medium by nano-sized zero-valent iron: a combination of oxidation and reduction, *J. Hazard. Mater.* 373 (2019) 417–424.
- [36] G.N. Zhou, W.Q. Li, C.S. He, X.C. Liu, R.R. Ding, Y.X. Wang, Y. Mu, Enhanced hydrodeiodination of iodinated contrast medium by sulfidemodified nano-sized zero-valent iron: Kinetics, mechanisms and application prospects, *Chem. Eng. J.* 401 (2020), 126050.
- [37] K.C. Christoforidis, M. Louloudi, E.R. Milaeva, Y. Deligiannakis, Mechanism of catalytic decomposition of pentachlorophenol by a highly recyclable heterogeneous SiO<sub>2</sub>-[Fe-porphyrin] catalyst, *J. Catal.* 270 (2010) 153–162.
- [38] J.M.J. Santillan, D.M. Arboleda, D.F. Coral, M.B. Fernandez van Raap, D. Muraca, D.C. Schinca, L.B. Scaffardi, Optical and magnetic properties of Fe nanoparticles fabricated by femtosecond laser ablation in organic and inorganic solvents, *ChemPhysChem* 18 (2017) 1192–1209.
- [39] L.Q. Wang, X. Lu, C. Han, R.E. Lu, S. Yang, X.P. Song, Electrospun hollow cage-like  $\alpha$ -Fe<sub>2</sub>O<sub>3</sub> microspheres: synthesis, formation mechanism, and morphology-preserved conversion to Fe nanostructures, *CrystEngComm* 16 (2014) 10618–10623.
- [40] D.J. Xiao, E.D. Bloch, J.A. Mason, W.L. Queen, M.R. Hudson, N. Planas, J. Borycz, A.L. Dzubak, P. Verma, K. Lee, F. Bonino, V. Crocella, J. Yano, S. Bordiga, D. G. Truhlar, L. Gagliardi, C.M. Brown, J.R. Long, Oxidation of ethane to ethanol by N<sub>2</sub>O in a metal-organic framework with coordinatively unsaturated iron(II) sites, *Nat. Chem.* 6 (2014) 590–595.
- [41] Y. An, Y. Liu, P.F. An, J.C. Dong, B.Y. Xu, Y. Dai, X.Y. Qin, X.Y. Zhang, M. H. Whangbo, B.B. Huang, NiII coordination to Al-based metal-organic framework made from 2-aminoterephthalate for photocatalytic overall water splitting, *Angew. Chem. Int. Ed.* 56 (2017) 3036–3040.
- [42] A. Fateeva, P.A. Chater, C.P. Ireland, A.A. Tahir, Y.Z. Khimyak, P.V. Wiper, J. R. Darwent, M.J. Rosseinsky, A water-stable porphyrin-based metal-organic framework active for visible-light photocatalysis, *Angew. Chem. Int. Ed.* 51 (2012) 7440–7444.
- [43] J.C. Munoz-Senmach, S. Kim, R.R. Arrieta-Perez, C.M. Park, Y.M. Yoon, A. J. Hernandez-Maldonado, Activated carbon-metal organic framework composite for the adsorption of contaminants of emerging concern from water, *ACS Appl. Nano Mater.* 3 (2020) 2928–2940.
- [44] M. Oveisi, N.M. Mahmoodi, M.A. Asli, Facile and green synthesis of metal-organic framework/inorganic nanofiber using electrospinning for recyclable visible-light photocatalysis, *J. Clean. Prod.* 222 (2019) 669–684.
- [45] R.R. Ding, W.Q. Li, C.S. He, Y.R. Wang, X.C. Liu, G.N. Zhou, Y. Mu, Oxygen vacancy on hollow sphere CuFe<sub>2</sub>O<sub>4</sub> as an efficient Fenton-like catalysis for organic pollutant degradation over a wide pH range, *Appl. Catal. B Environ.* 291 (2021), 120069.
- [46] S.E. Lehman, A.S. Morris, P.S. Mueller, A.K. Salem, V.H. Grassian, S.C. Larsen, Silica nanoparticle-generated ROS as a predictor of cellular toxicity: mechanistic insights and safety by design, *Environ. Sci. Nano* 3 (2016) 56–66.
- [47] J.M. Lazaro-Martinez, L.V.L. Lupano, L.L. Piehl, E. Rodriguez-Castellon, V.C. D. Orto, New insights about the selectivity in the activation of hydrogen peroxide by cobalt or copper hydrogel heterogeneous catalysts in the generation of reactive oxygen species, *J. Phys. Chem. C* 120 (2016) 29332–29347.
- [48] T. Guo, L.S. Jiang, K. Wang, Y. Li, H.X. Huang, X.Y. Wu, G.K. Zhang, Efficient persulfate activation by hematite nanocrystals for degradation of organic pollutants under visible light irradiation: facet-dependent catalytic performance and degradation mechanism, *Appl. Catal. B Environ.* 286 (2021), 119883.
- [49] Q.S. Wu, H.P. Yang, L. Kang, Z. Gao, F.F. Ren, Fe-based metal-organic frameworks as Fenton-like catalysts for highly efficient degradation of tetracycline hydrochloride over a wide pH range: acceleration of Fe(II)/Fe(III) cycle under visible light irradiation, *Appl. Catal. B Environ.* 263 (2020), 118282.
- [50] X. Hu, X.J. Hu, Q.Q. Peng, L. Zhou, X.F. Tan, L.H. Jiang, C.F. Tang, H. Wang, S. H. Liu, Y.Q. Wang, Z.Q. Ning, Mechanisms underlying the photocatalytic degradation pathway of ciprofloxacin with heterogeneous TiO<sub>2</sub>, *Chem. Eur. J.* 380 (2020), 122366.
- [51] X.H. Yi, H.D. Ji, C.C. Wang, Y. Li, Y.H. Li, C. Zhao, A.O. Wang, H.F. Fu, P. Wang, X. Zhao, W. Liu, Photocatalysis-activated SR-AOP over PDINH/MIL-88A(Fe) composites for boosted chloroquine phosphate degradation: performance, mechanism, pathway and DFT calculations, *Appl. Catal. B Environ.* 293 (2021), 120229.
- [52] F. Chen, L.L. Liu, Y.J. Zhang, J.H. Wu, G.X. Huang, Q. Yang, J.J. Chen, H.Q. Yu, Enhanced full solar spectrum photocatalysis by nitrogen-doped graphene quantum dots decorated BiO<sub>2-x</sub> nanosheets: ultrafast charge transfer and molecular oxygen activation, *Appl. Catal. B Environ.* 277 (2020), 119218.
- [53] C.H. Hendon, D. Tiana, M. Fontecave, C. Sanchez, L. D'arras, C. Sasso, L. Rozes, C. Mellot-Draznics, A. Walsh, Engineering the optical response of the titanium-MIL-125 metal-organic framework through ligand functionalization, *J. Am. Chem. Soc.* 135 (2013) 10942–10945.
- [54] Z. Jiang, X. Xu, Y.H. Ma, H.S. Cho, D. Ding, C. Wang, J. Wu, P. Oleynikov, M. Jia, J. Cheng, Y. Zhou, O. Terasaki, T.Y. Peng, L. Zan, H.X. Deng, Filling metal-organic framework mesopores with TiO<sub>2</sub> for CO<sub>2</sub> photoreduction, *Nature* 586 (2020) 549–554.
- [55] C.Y. Xu, Y. Pan, G. Wan, H. Liu, L. Wang, H. Zhou, S.H. Yu, H.L. Jiang, Turning on visible-light photocatalytic C-H oxidation over metal-organic frameworks by introducing metal-to-cluster charge transfer, *J. Am. Chem. Soc.* 141 (2019) 19110–19117.
- [56] J. Wang, J. Zhang, Y.Z. Zhou, H.B. Liu, Q.F. Xue, X.S. Li, C.C. Chueh, H.L. Yip, Z. L. Zhu, A.K.Y. Jen, Highly efficient all-inorganic perovskite solar cells with suppressed non-radiative recombination by a Lewis base, *Nat. Commun.* 11 (2020) 1–9.
- [57] Q.J. Xiang, J. Yu, M. Jaroniec, Synergetic effect of MoS<sub>2</sub> and graphene as cocatalysts for enhanced photocatalytic H<sub>2</sub> production activity of TiO<sub>2</sub> nanoparticles, *J. Am. Chem. Soc.* 134 (2012) 6575–6578.
- [58] H.X. Huang, T. Guo, K. Wang, Y. Li, G.K. Zhang, Efficient activation of persulfate by a magnetic recyclable rape straw biochar catalyst for the degradation of tetracycline hydrochloride in water, *Sci. Total Environ.* 758 (2021), 143957.
- [59] A.J. Clough, N.M. Orchanian, J.M. Skelton, A.J. Neer, S.A. Howard, C.A. Downes, L.F.J. Piper, A. Walsh, B.C. Melot, S.C. Marinescu, Room temperature metallic conductivity in a metal-organic framework Induced by oxidation, *J. Am. Chem. Soc.* 141 (2019) 16323–16330.
- [60] Z.Z. Wang, L.S. Jiang, K. Wang, Y. Li, G.K. Zhang, Novel AgI/BiSbO<sub>4</sub> heterojunction for efficient photocatalytic degradation of organic pollutants under visible light: interfacial electron transfer pathway, DFT calculation and degradation mechanism study, *J. Hazard. Mater.* 410 (2021), 124948.
- [61] I. Grigioni, M. Abdellah, A. Corti, M.V. Dozzi, L. Hammarström, E. Selli, Photoinduced charge-transfer dynamics in WO<sub>3</sub>/BiVO<sub>4</sub> photoanodes probed through midinfrared transient absorption spectroscopy, *J. Am. Chem. Soc.* 140 (2018) 14042–14045.
- [62] K. Sato, R. Katoh, Fluorescence properties of  $\beta$ -perylene crystals prepared by a physical vapor transport method under atmospheric pressure, *Chem. Phys. Lett.* 730 (2019) 312–315.